

ACCEPTED MANUSCRIPT

@(®)

Characterizing brain mechanics through 7 Tesla magnetic resonance elastography

To cite this article before publication: Emily Triolo et al 2024 Phys. Med. Biol. in press https://doi.org/10.1088/1361-6560/ad7fc9

Manuscript version: Accepted Manuscript

Accepted Manuscript is "the version of the article accepted for publication including all changes made as a result of the peer review process, and which may also include the addition to the article by IOP Publishing of a header, an article ID, a cover sheet and/or an 'Accepted Manuscript' watermark, but excluding any other editing, typesetting or other changes made by IOP Publishing and/or its licensors"

This Accepted Manuscript is © 2024 Institute of Physics and Engineering in Medicine. All rights, including for text and data mining, Al training, and similar technologies, are reserved..

During the embargo period (the 12 month period from the publication of the Version of Record of this article), the Accepted Manuscript is fully protected by copyright and cannot be reused or reposted elsewhere.

As the Version of Record of this article is going to be / has been published on a subscription basis, this Accepted Manuscript will be available for reuse under a CC BY-NC-ND 3.0 licence after the 12 month embargo period.

After the embargo period, everyone is permitted to use copy and redistribute this article for non-commercial purposes only, provided that they adhere to all the terms of the licence https://creativecommons.org/licences/by-nc-nd/3.0

Although reasonable endeavours have been taken to obtain all necessary permissions from third parties to include their copyrighted content within this article, their full citation and copyright line may not be present in this Accepted Manuscript version. Before using any content from this article, please refer to the Version of Record on IOPscience once published for full citation and copyright details, as permissions may be required. All third party content is fully copyright protected, unless specifically stated otherwise in the figure caption in the Version of Record.

View the article online for updates and enhancements.

Title: Characterizing Brain Mechanics Through 7 Tesla Magnetic Resonance Elastography

Authors: E.R. Triolo*†, O. Khegai*, M. McGarry, T. Lam, J. Veraart, A. Alipour, P. Balchandani, and M. Kurt

*E.R. Triolo and O. Khegai contributed equally to this work

[†]E.R. Triolo is the Corresponding Author

Affiliations:

- E.R. Triolo (e-mail: etriolo@uw.edu) and T. Lam (e-mail: tysonlam@uw.edu) are with the Dept. Mechanical Engineering, University of Washington, Seattle, WA USA.
- O. Khegai (e-mail: oleksandr.khegai@mssm.edu), A. Alipour (e-mail: akbar.alipour@mssm.edu), and P. Balchandani (e-mail: priti.balchandani@mssm.edu), are with The Biomedical Engineering and Imaging Institute, Icahn School of Medicine at Mount Sinai, New York City, NY, USA.
- M. McGarry (e-mail: matthew.d.mcgarry@dartmouth.edu) is with the Thayer School of Engineering, Dartmouth College, Hanover, NH, USA
- J. Veraart is with Center for Biomedical Imaging, Dept. Radiology, New York University Grossman School of Medicine, New York City, NY, USA (e-mail: Jelle.Veraart@nyulangone.org)
- M. Kurt is with the Dept. Mechanical Engineering, University of Washington, Seattle, WA USA and The Biomedical Engineering and Imaging Institute, Icahn School of Medicine at Mount Sinai, New York City, NY, USA. (e-mail: mkurt@uw.edu)



Abstract

Magnetic resonance elastography (MRE) is a non-invasive method for determining the mechanical response of tissues using applied harmonic deformation and motion-sensitive MRI. MRE studies of the human brain are typically performed at conventional field strengths, with a few attempts at the ultra-high field strength, 7T, reporting increased spatial resolution with partial brain coverage. Achieving high-resolution human brain scans using 7T MRE presents unique challenges of decreased octahedral shear strain-based signal-to-noise ratio (OSS-SNR) and lower shear wave motion sensitivity. In this study, we establish high resolution MRE at 7T with a custom 2D multi-slice single-shot spin-echo EPI sequence, using the Gadgetron advanced image reconstruction framework, applying Marchenko-Pastur Principal Component Analysis denoising, and using Nonlinear Viscoelastic Inversion. These techniques allowed us to calculate the viscoelastic properties of the whole human brain at 1.1 mm isotropic imaging resolution with high OSS-SNR and repeatability. Using phantom models and 7T MRE data of eighteen healthy volunteers, we demonstrate the robustness and accuracy of our method at highresolution while quantifying the feasible tradeoff between resolution, OSS-SNR, and scan time. Using these post-processing techniques, we significantly increased OSS-SNR at 1.1 mm resolution with wholebrain coverage by approximately 4-fold and generated elastograms with high anatomical detail. Performing high-resolution MRE at 7T on the human brain can provide information on different substructures within brain tissue based on their mechanical properties, which can then be used to diagnose pathologies (e.g., Alzheimer's disease), indicate disease progression, or better investigate neurodegeneration effects or other relevant brain disorders, in vivo.

Keywords: Magnetic Resonance Elastography, Magnetic Resonance Imaging, Ultra-High Field MRI, Human Brain, Mechanical Properties, Signal Processing



Introduction

Historically, pathologies such as tumors or lesions have been identified by physicians by manually palpating soft tissue to compare the mechanical properties of healthy tissue to potentially malignant tissues. However, this technique is not practical for certain internal organs such as the brain, where direct manual examination is not feasible. Therefore, it was necessary to develop a method for noninvasive tissue stiffness estimation and quantification, such as Magnetic Resonance Elastography (MRE) [1]. MRE utilizes mechanical tissue deformation and employs magnetic resonance imaging (MRI) as a method to detect and quantify the motion within the tissue [2]. This process involves applying force to the tissue, with various methods available for this purpose. The most common approach in MRE is to induce controlled harmonic vibration, which allows for the measurement of tissue response to mechanical harmonic deformation [3]. Viscoelastic models are used to extract structural information from MRE measurements by establishing a mathematical relationship between viscoelastic parameters of tissue and its mechanical response to the applied harmonic vibration. Performing MRE on the human brain can provide information on different structures within brain tissue based on their mechanical properties, such as cell density, myelination, inflammation, and vascular density [4], [5], [6], [7], [8], [9], [10], [11], [12], [13], [14], [15], [16], [17], [18], [19], [20]. These mechanical parameters can then be used as biomarkers to diagnose pathologies such as multiple sclerosis, Alzheimer's disease, and Parkinson's disease, or indicate disease progression [10], [21], [22], [23], [24], [25], [26], [27], [28], [29]. One potential and impactful avenue for improvement of MRE in brain tissue is image resolution, which typically ranges between 1.25-3.00 mm² in-plane resolution [4], [6], [7], [8], [10], [15], [16], [18], [21], [22], [23], [24], [25], [26], [27], [28], [29], [30], [31], [32], [33], [34], [35], [36], [37], [38]. Enhancing this aspect of MRE acquisition could improve the specificity in determining the underlying microstructural changes that result in alterations of viscoelastic parameters. While there are multiple methods of potentially tackling this matter, moving from conventional field strengths (1.5T or 3T) to the ultra-high field strength, 7T, is a promising option as human 7T scanners have an increasing availability in the clinical environment.

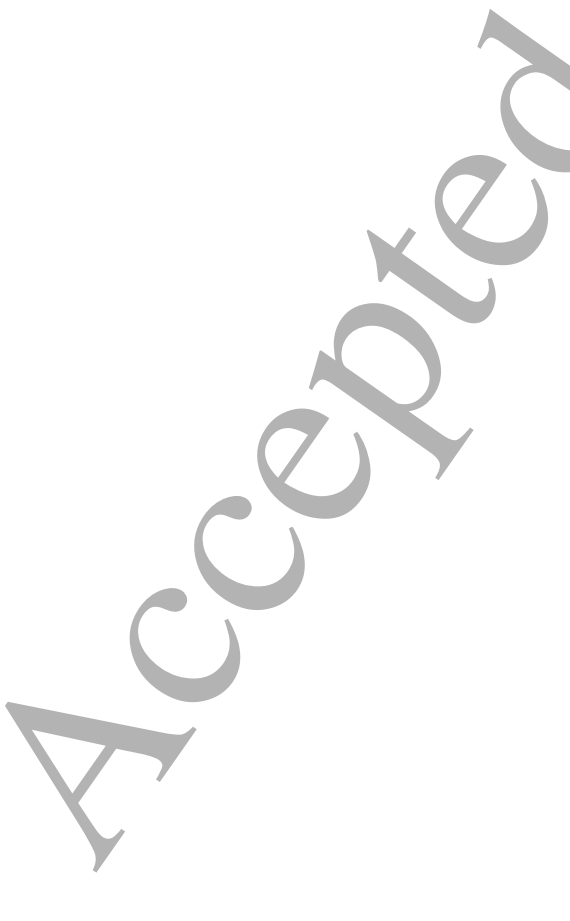
Compared to 3T scans, 7T MRI offers a higher signal-to-noise (SNR), resulting in enhanced spatial resolution [39]. High resolution MRE will be imperative for clinical applicability to diseases and disorders of the human brain that affect small regions, such as the subfields of the hippocampus. Additionally, in tissues apart from the brain where higher frequency actuation can be used, this higher resolution that can only be achieved at 7T must be used to capture enough points along the shear wavelength for a stable inversion [40], [41], [42]. While SNR theoretically scales with field strength, 7T MRE suffers from B_0 and B_1 inhomogeneities that need to be addressed with advanced shimming techniques. Additionally, at higher magnetic field strengths spin-spin relaxation effects occur faster resulting in a decreased apparent T_2 (T_2 *) value for tissue, and therefore requiring a shorter echo time (TE) to better match the T_2 * and reduce signal

dropout. This presents a unique challenge in MRE, as the required TE is longer than most other MRI sequences to accommodate the additional motion encoding gradient (MEG), leading to SNR and magnitude degradation in MRE more than other 7T sequences. Due to these challenges and the current novelty of 7T human MRI scanners, there have only been a handful of studies investigating 7T MRE. The first published study performing 7T MRE of the human brain was a single-subject feasibility study comparing MRE at 1.5T to MRE at the same resolution at 7T for partial brain coverage [34]. While this study proved the feasibility of MRE at 7T, it did not consider potential differences in SNR or increased resolution at 7T. This was attributed to more pronounced susceptibility artifacts and greater T₂* spatial variation and signal decay. The following 7T MRE studies investigating the human brain were also partial-brain acquisition only, and although high-resolution was implemented, these studies still suffered from the same drawbacks, e.g., signal dropout, and distortions [43]. Additionally, the reported values of shear stiffness at 7T were much lower than that of other literature values, at a gray matter average of 0.98 kPa [43] as compared to 2.01, 2.41, or 3.77 kPa at 3T or 1.5T [44] in studies with comparable methods apart from resolution and field strength. This difference in shear stiffness between resolutions/field strengths was also noted, and this difference was determined to be statistically significant, in the subsequent studies. These studies investigated a larger cohort at 1.5T, 3T, and 7T, although these studies did not collected data at matched imaging resolutions and relied on down-sampling in an effort to distinguish between the effect of resolution and the effect of field strength on shear stiffness [45], [46]. While motion corrections were successful at 7T, distortion and field inhomogeneity corrections were challenging, despite their implementation at 3T [47]. Subsequent investigations have also found potential differences in estimated quantitative values between 1.5T, 3T, and 7T MRE, although these studies did not control for resolution or include phantom validation, and used a direct inversion method which has limited accuracy at higher resolutions [45], [46].

Despite these challenges, 7T MRE has shown promise in more recent pilot studies as a method of obtaining high-resolution quantitative viscoelastic parameters of the human brain [34], [43], [46], [48], [49], [50], [51]. At conventional field strengths, MRE has been shown to be sensitive to changes in whole brain viscoelasticity due to healthy brain development and aging, as well as changes due to neurodegeneration [10], [23], [24]. By exploiting the high spatial resolution possible at 7T, we can potentially increase this sensitivity to show more subtle changes in viscoelasticity and pinpoint changes in smaller brain sub-structures by reducing partial volume effects. However, aiming for higher imaging resolution of the human brain at 7T, MRE presents unique challenges of decreased octahedral shear strain-based SNR (OSS-SNR) and lower shear wave motion sensitivity. Despite this, while encoding efficiency primarily depends on effective dephasing caused by MEG amplitude and duration, higher SNR at 7T leads to a more correct estimation of the phase difference. Additionally, it has been shown at 3T that quantitative values of MRE, *i.e.*, the shear stiffness, are sensitive to changes in OSS-SNR [52], so 7T MRE can present

a challenge of not only quality, but accuracy. While applying commonly-used filtering techniques (*e.g.*, Gaussian, Median, Wavelet Thresholding, Reduced Energy Ratio, directional filtering) [48], [53], [54], [55], [56], [57], [58] to MRE imaging data can increase SNR and OSS-SNR (to combat low SNR in high-resolution scans), this can also blur fine physiological features, decrease the effective resolution [59], resulting in artificially increased stiffness estimates [52].

Another complication at 7T, particularly at high-resolution, is image reconstruction error related to phase wrapping when using scanner-reconstructed images. While advanced reconstruction options are available on some MRI scanners, they are typically not optimized for reconstructing phase images. Millimeter or sub-millimeter echo-planar imaging (EPI) using conventional reconstruction algorithms introduces irregularities and wrapping effects in the phase images that can bias the MRE inversion reconstruction [49], [50], [60]. To provide repeatable viscoelastic properties of brain tissue at high-resolution, the acquired 7T MRE images must have sufficient amplitude of the motion encoded, be reconstructed from the Fourier *k*-space in a manner to remove phase irregularities, and denoised without over-smoothening and losing anatomical structure. In this study, we will establish high resolution of whole brain coverage MRE at 7T with a target of 1 mm isotropic resolution, in addition to demonstrating the advanced post-processing techniques of Marchenko-Pastur Principal Component Analysis (MP-PCA) denoising [59], Gadgetron image reconstruction framework [61], and Nonlinear Viscoelastic Inversion [42] to calculate the viscoelastic properties of the human brain while considering the tradeoff between resolution, OSS-SNR, and scan time.



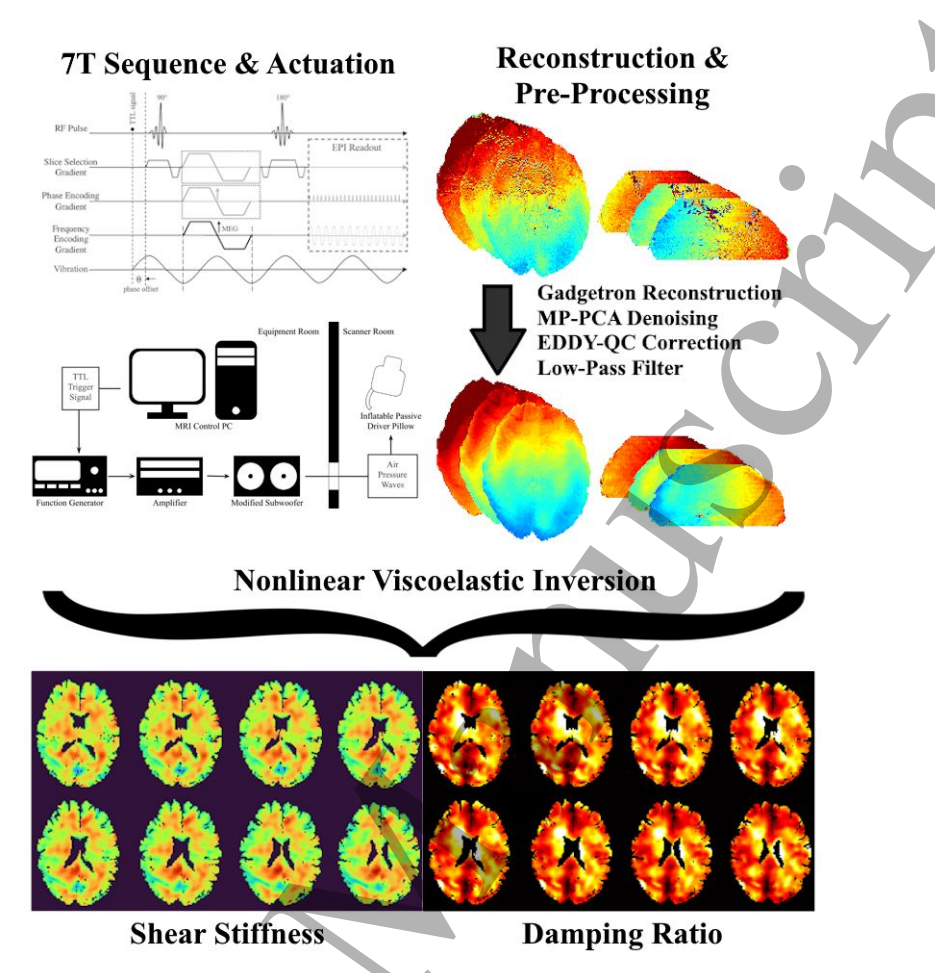


Figure 1. Methodological Overview of 7T MRE. A custom 7T MRE pneumatic actuator and sequence are used to produce and capture the motion of the human brain, encoded in the phase. A post-processing procedure to remove phase wrapping error, spatially varying noise, and subject motion was used prior to nonlinear inversion to calculate the shear stiffness and damping ratio of the human brain.

Materials and Methods

7T MRE Sequence Parameter Optimization

A previous MRI study revealed that the enhancement of SNR due to magnetic field strength varies depending on the position within the head. SNR increases approximately linearly for voxels located near the surface of the head. However, for voxels deep within the brain, the increase is more than linear. Specifically, for voxels near the center of the head, the SNR increases roughly with a power factor B_0^x , where x is approximately 2.1; whereas near the surface, x is only approximately 1.2 [62]. This inhomogeneity affects average image SNR, but can be addressed using decreased voxel volumes, shimming, and collecting reference volumes in opposite phase encoding directions so the distortions are in opposite directions and can be filtered out [63]. B_1 inhomogeneity also increases with field strength [39], as the B_1 operating wavelength gets closer to the dimension of the tissue of interest (in this case the human

head) as B_0 increases [64]. This results in decreased B_1 efficiency at the periphery of the tissue compared to the center, with peripheral B_1 being 42% lower than central B_1 [64]. This leads to changes in contrast and signal drop-out across the image, and conventional pulse sequences are particularly susceptible to this B_1 inhomogeneity.

As mentioned previously, in addition to increased B_o and B_1 inhomogeneities, at higher magnetic field strengths, relaxation effects occur faster, resulting in a decreased apparent T_2 (T_2*) value [64]. For example, for the gray matter in the brain, while T_2 at 3T is 80 ms, at 7T, T_2 is only 42 ms [65]. This results in a unique problem not addressed at conventional field strengths, and that is making the TE of a sequence close enough to the T_2 or T_2* value to preserve SNR and signal amplitude. Long TEs make a sequence more sensitive to signal relaxation, therefore, a longer TE compared to the relaxation constant results in lower SNR [66]. However, in MRE, the length of the required TE is longer than most other MRI sequences in order to accommodate the MEG, leading to SNR and amplitude degradation in MRE more than other 7T sequences. An EPI pulse sequence is useful for such an application because it can acquire a necessary volume of data with short acquisition times.

The modified 2D multi-slice single-shot spin-echo EPI sequence (Figure 2) was designed to acquire MRE data using phase shifted bipolar or trapezoidal flow-compensated 3D motion-encoding gradients (MEGs) synchronized with the acoustic actuator by TTL triggering. Data was acquired in an interleaved fashion to reduce distortion artifacts. Additionally, we used acceleration techniques such as GRAPPA (GeneRalized Autocalibrating Partial Parallel Acquisition) and partial Fourier to reduce TE to the minimal value required for accommodating MEGs [67]. We also investigated the difference between bipolar and flow-compensated MEGs. The switch to flow-compensated MEGs from bipolar resulted in more symmetric encoding of wave propagation by removing artifacts that resulted from physiological motion and avoiding flow-related dephasing cause by cerebral blood from, and therefore improved complex shear modulus estimates.

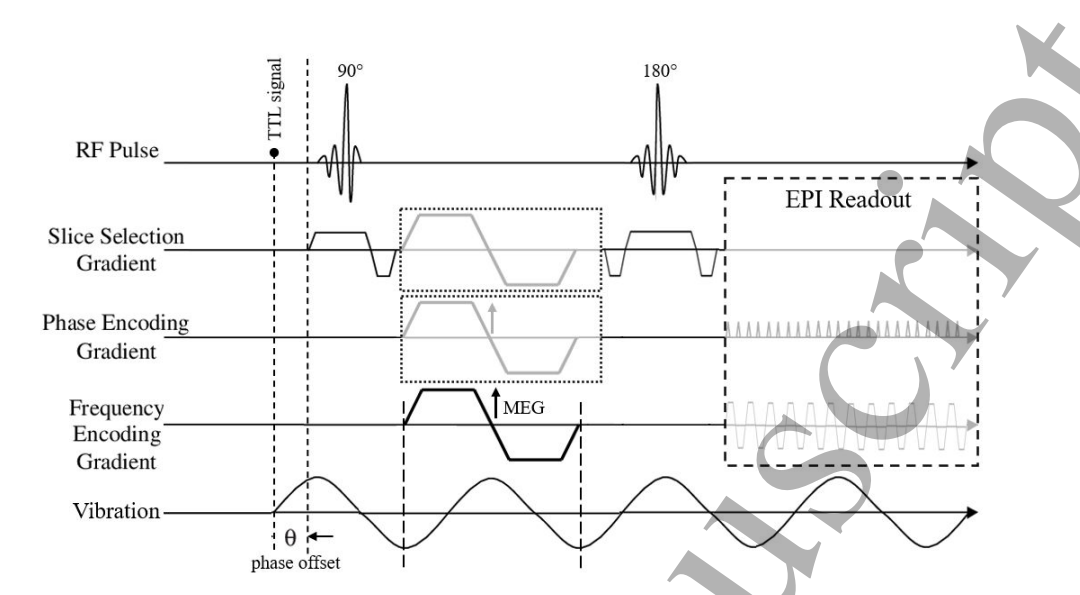


Figure 2. Custom 7T MR Elastography sequence diagram with bipolar MEGs applied consecutively on frequency, phase and slice encoding directions.

Data Acquisition, Post-Processing, Inversion, and SNR Calculation

The ultra-high field data were acquired on 7T whole-body MRI scanner (Magnetom 7T, Siemens Healthineers, Germany) equipped with a 70 mT/m gradient coil and a 32-channel head coil (Nova Medical, Wakefield, MA). After each scanning session, both the raw data and DICOM image series for the MRE scans were collected. Using the raw data, we perform post-hoc offline reconstruction of magnitude and phase images using an open-source Gadgetron image reconstruction framework [61] to remove artifacts caused by scanner reconstruction error, such as inaccurate value assignment in pixels along phase wrapping lines. Gadgetron implements advanced reconstruction techniques that are not typically used in scanners due to long computation time. Specifically in this study, we are using advanced coil combination based on a non-linear optimization scheme [68], [69]. To remove spatially varying noise in our MRE acquisition without comprising the anatomical accuracy and spatial resolution, we utilize an MP-PCA denoising algorithm [59]. In this technique, originally applied for denoising diffusion-weighted images, we are exploiting the intrinsic redundancies in MRE acquisition to identify and remove noise-only principal components [59]. Specifically, we can exploit the redundancies across the MRE acquisition (N=48; 2 encoding directions, 3 orthogonal MEG directions, 8 phase offsets) and the universal properties of the eigenspectrum of random covariance matrices to identify and remove noise-only principal components. We can therefore identify and remove the pure noise eigenvalues by estimating noise level and number of significant signal components based on an MP distribution, resulting in our denoised matrix. Thereby, one increases precision and SNR without compromising physiological accuracy and spatial resolution. We employed the MP-PCA denoising algorithm to complex signal in a $5 \times 5 \times 5$ sliding block.

The difference was then taken between two phase images acquired with reversed MEGs and unwrapped using SEGUE unwrapping [70]. Using the denoised Gadgetron reconstructed magnitude images for each image series, we used FSL's EDDY framework [71] to perform motion correction on these magnitude images, as well as use EDDY QC to generate a subject motion report for each acquisition for each subject. While EDDY does not have the capability to perform motion corrections on phase data, we were able to use the subject motion report to correct changes in phase that results from significant subject motions (above 2 standard deviations of average subject motion). While interleaved acquisition is useful in EPI sequences for reducing distortion, subject motion may cause a 'z-striping' effect where reference phase is only altered due to small subject motion in every other slice. After removing large outliers based on the EDDY OC motion report, we employed a simple low-pass 4th-order Butterworth filter to remove the highfrequency striping effect that occurs due to small, irregular subject motions. In extreme striping cases, we also used the motion report to estimate the approximate phase in these slices as if the subject had not moved. Finally, Nonlinear Viscoelastic Inversion was used to calculate the commonly reported metrics, shear stiffness (μ , equation 1) and damping ratio (ξ , equation 2) from the denoised and motion-corrected unwrapped displacement data, where G' is the storage modulus, G" is the loss modulus, and G*=G'+iG''[42].

$$\mu = \frac{2|G^*|^2}{(G'+|G^*|)}$$
 [1]
$$\xi = \frac{G''}{2G'}$$
 [2]

We also calculated OSS-SNR for each image series. To do this, we used the displacement as calculated during pre- processing (SEGUE unwrapped phase difference multiplied by the MENC value) before using Fourier decomposition to extract the different harmonic displacements. We then calculated OSS [72] of only the main harmonic component and the OSS of the sum of the other harmonic components. The ratio of the main harmonic component OSS to the OSS of the other harmonics is used as the OSS-SNR of the scan and data processing method. Whole brain, white matter, and gray matter binary masks were generated using SPM12 [73] using an MP2RAGE T1-weighted whole-brain acquisition (0.7 mm isotropic resolution, TE/TR = 3.62/6000 ms) for each subject, and the resulting masks and T1 structural images were then co-registered with the motion-corrected magnitude images captured during MRE acquisition. The masks were used to segment elastograms and OSS-SNR maps to calculate whole brain, gray matter, and white matter averages.

Phantom Validation Scans

To validate the developed MRE sequence at the resolutions of interest with high SNR and OSS-SNR, we performed experiments on a custom elasticity MRE phantom (CIRS 049, CIRS, USA) with the manufacturer's specifications of a background Young's modulus of 5.0±1.0 kPa and spherical inclusions of 3.00±1.00 kPa, 8.00±1.00 kPa, 12.00±2.00 kPa, and 20.00±2.00 kPa Young's Modulus (Fig 3(a), background shear stiffness of 1.70±0.30 kPa and spherical inclusions of 1.00±0.30 kPa, 2.70±0.30 kPa, 4.00±0.70 kPa, and 6.70±0.70 kPa Shear Modulus). MRE acquisition was performed at 7T using our custom multi-slice 2D-EPI pulse sequence with 3D MEGs [74], a vibration frequency of 50 Hz and 8 phase offsets at 2.5 mm, 1.7 mm, and 1.1 mm isotropic imaging resolutions. The authors would like to note that when referring to 'resolution' in this work, we are referring to imaging resolution and not resolution of elastographic detail, of which the numerical value is difficult to exactly determine and is dependent on inversion technique [75].

To obtain a similar vibration amplitude and OSS-SNR, low amplitudes of vibration were used by adjusting the input voltage to one of two relatively low levels. To obtain a comparable image SNR to that of human scans, a lower excitation flip angle of 35° was used. External vibration was applied to the surface of the phantom using a custom pneumatic actuator described in Triolo, *et al.* [49], [50], [51], [76]. Elastograms and OSS-SNR maps of the phantom's cross section were obtained using the post-processing methods described previously. The average of each elastogram and OSS-SNR map of five homogeneous slices per scan (2.5 mm, 1.7 mm, and 1.1 mm) were compared. An ROI around the 1.00 kPa and 2.70 kPa shear stiffness spherical inclusions were also drawn to compare accuracy of small structures at each resolution.

Human Scans

This study and protocol was approved by the local Institutional Review Board, and written informed consent was obtained from all participants prior to the investigation. Full brain coverage MRE at 2.5 mm, 1.7 mm, and 1.1 mm isotropic resolution was performed on eighteen healthy volunteers (Average age 27.5 ± 3.6 years old, 9F, 9M) at 7T using previously described MRE pulse sequence, a vibration frequency of 50 Hz and 8 phase offsets with the sequence parameters listed in Table 1. One of these subjects was scanned at each of the three full-brain coverage resolutions three times over the course of one week in order to test repeatability (twice in one day and once on a different day). Informed consent was obtained from all participants for being included in the study. Full brain coverage MRE was also performed on sixteen of the same subjects on a 3T Siemens Skyra scanner with a 16-channel head coil (Siemens Healthineers) at 2.5 mm isotropic resolution using an echo planar spin echo 2D pulse sequence with vibration frequency 50 Hz, TE = 70 ms, TR = 5600 ms, GRAPPA = 3. Three of the subjects in this cohort

also underwent a 0.8 mm isotropic resolution partial-brain MRE scan on the 7T scanner at a vibration frequency of 50 Hz and 8 phase offsets to demonstrate the feasibility of sub-millimeter 7T MRE.

Table 1. Sequence	Parameters for	Whole Brain Coverage H	uman MRE Scans at 7T

Resolution	TE	TR	GRAPPA	Partial Fourier	# of Slices	Scan Duration (mm:ss)
2.5 mm	65 ms	4800 ms	2	N/A	40	04:05
1.7 mm	65 ms	7200 ms	2	N/A	60	06:07
1.1 mm	65 ms	14000 ms	3	7/8	100	12:22
0.8 mm	70 ms	5120 ms	3	7/8	32	04:31

Vibration was applied to the head via the custom pneumatic actuator, using the final 3D printed thermoplastic polyurethane (TPU, a flexible 3D printing filament material) end-effector shaped to rest in the base of the head coil, the construction and validation of which is described in Triolo, *et al.* [76] Elastograms and OSS-SNR maps of each of the scans were obtained using the processing methods described above, but scanner reconstructed images were processed from the 3T data instead of the raw data files. Repeated measures ANOVA with Bonferroni correction and multiple comparisons was performed between each group of resolutions and field strengths to determine statistical significance while accounting for inter-subject variation. To investigate the similarity between the 3T and 7T datasets at matched resolution, we also calculated the average Structural Similarity Index (SSIM), a method for measuring the similarity between two images, as defined by:

SSIM
$$(x,y) = \frac{(2\mu_x\mu_y + c_1)(2\sigma_{xy} + c_2)}{(\mu_x^2 + \mu_y^2 + c_1)(\sigma_x^2 + \sigma_y^2 + c_2)}$$
 [3]

where μ_x is the voxel-by-voxel mean of x (*i.e.*, MRE 3T elastograms), μ_y is the voxel-by-voxel mean of y (*i.e.*, MRE 7T elastograms), σ_x^2 is the spatial variance of x, σ_y^2 is the spatial variance of y, σ_{xy} is the spatial covariance of x and y, and the c's are stabilization variables. MATLAB was used to perform this analysis, so the structural similarity for each pixel is based on its relationship to other pixels in an 11-by-11 window. This metric has been historically used to compare between reconstruction and undersampling methods in MRE studies to ensure that those acceleration methods do not degrade image quality or introduce significant artifacts [77], [78]. Therefore, SSIM was determined as an appropriate metric for determining the structural similarities between our imaging metric maps of matched resolution. However, the different acquisition resolutions have not been compared with SSIM analysis. In order to reduce any bias by up-sampling and interpolating low resolution data or down-sampling high resolution data, we only used SSIM to compare between the images of matched resolution.

Using the MP2RAGE T1-weighted images acquired for each subject, Freesurfer 7.0 segmentation was performed, and masks for each region of interest (whole brain left hemisphere, whole brain right

hemisphere, caudate, corpus callosum, hippocampus, putamen, and thalamus) were generated based on each individual's parcellation. The T1 structural image and resulting masks were co-registered and resliced to the MRE magnitude space for each resolution and field strength using SPM12 [73]. Regional average stiffness and damping ratio, percent difference in stiffness and damping ratio between gray matter and white matter, percent difference in stiffness and damping ratio between left hemisphere and right hemisphere, and stiffness contrasts [41] (between small regions and gray matter, small regions and white matter, and between the caudate and putamen) were calculated for each individual. Paired t-tests were used to compare between left and right hemispheres and Cohen's-d was calculated to determine effect size (reported in Supplementary Materials). Prior to all ANOVA and t-tests performed, a Shapiro Wilk test was performed to ensure that the data are normally distributed, and correction has been applied if necessary for the t-tests. No normality corrections were performed for between-group analyses performed with ANOVAs, however, as it is considered a robust test against the normality assumption.

Results

Phantom Validation Scans

In phantom validation scans with lowered SNR and OSS-SNR values, similar to the human scans, the estimated shear modulus values were within the specification range given by the phantom's data sheet (1.70±0.30 kPa). There was also no significant difference in shear modulus found between any of the resolution groups (p>0.50). This would indicate that in a homogeneous, linearly elastic material, changing resolution does not inherently change the calculated shear stiffness of the material being imaged. Furthermore, moving from 2.5 mm resolution to 1.1 mm resolution results in shear modulus estimates of the spherical inclusions that match the manufacturer specifications of the custom MRE phantom.

At 2.5 mm resolution, the inclusion in the specification range 1.00 ± 0.30 kPa Shear modulus is within the specified range at 0.85 ± 0.17 kPa, but the inclusion of specification range 2.70 ± 0.30 kPa is not in the correct range at only 1.74 ± 0.24 kPa. At 1.1 mm resolution, the lower stiffness inclusion was calculated to have shear stiffness in the correct ranges at 0.82 ± 0.12 kPa, and the stiffer inclusion was closer to the lower end of the manufacturer specified range at 2.12 ± 0.07 kPa (Fig 3(b)). Despite not being exactly within the manufacturer's specifications, the estimate aligns with the trend of the material properties of the phantom being on the softer side of what was specified. This alteration in measured shear stiffness in the stiffer spherical inclusion, as well as the lowered standard deviation at higher resolution, implies that increasing resolution results in more accurate shear stiffness calculations for smaller features, such as these inclusions. Additionally, this apparent softer stiffness measurement than expected based on specifications is similarly observed in Herthum, *et al.*, in which softer inclusions were more accurately estimated than stiffer ones, as was expected based on the finite-differences schemes used by inversion methods [79].

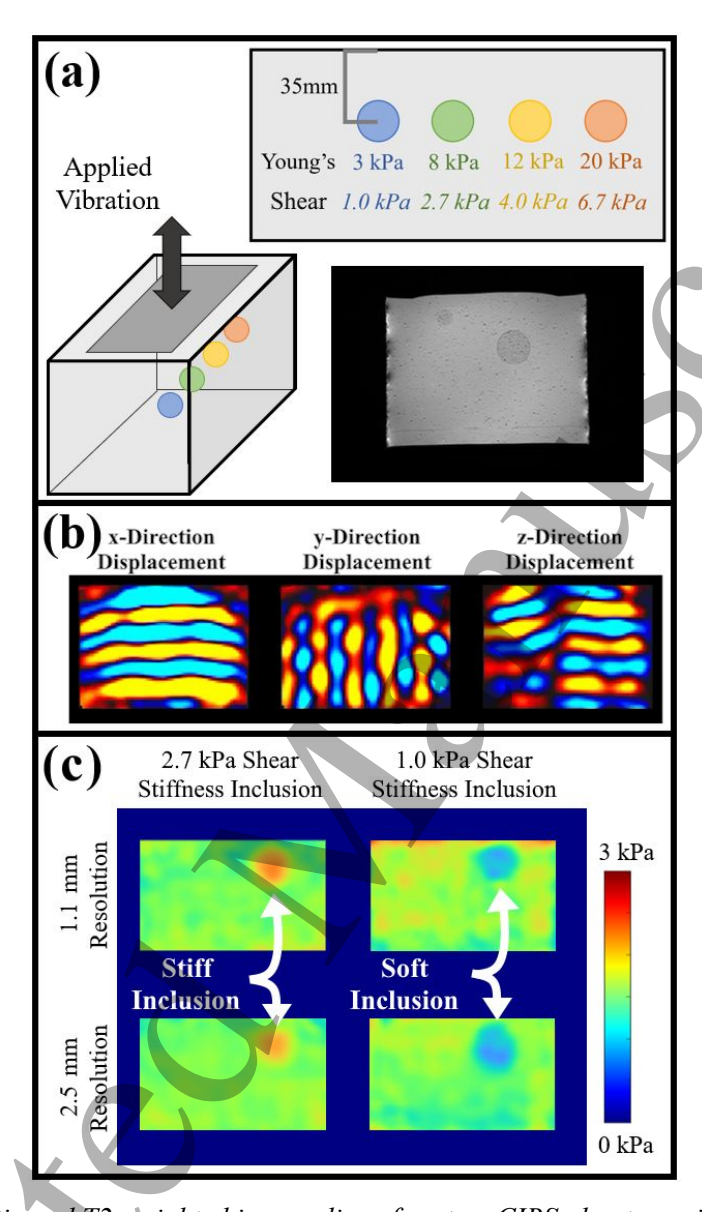


Figure 3. (a) Schematic and T2-weighted image slice of custom CIRS phantom with a background shear of 1.7 kPa and multiple spherical inclusions (listed as both Young's Modulus values and shear modulus), (b) normalized displacement in a homogeneous slice of the custom phantom shown at 1.1 mm resolution in all three orthogonal directions, and (c) 1.1 mm and 2.5 mm resolution elastograms in the custom phantom in slices with the 2.70±0.30 kPa shear modulus (measured as 2.12±0.07 kPa shear stiffness in 1.1 mm resolution scan and 1.74±0.24 kPa in 2.5 mm resolution scan) and 1.00±0.30 kPa shear stiffness (measured as 0.82±0.12 kPa shear stiffness in 1.1 mm resolution scan and 0.85±0.17 kPa in 2.5 mm resolution scan) spherical inclusions

Human Scans

We successfully performed MRE at 7T on all subjects at all resolutions and reconstructed the data using nonlinear inversion (Figure 4). By applying Gadgetron reconstruction and MP-PCA denoising to the 7T data, we observed a statistically significant increase in OSS-SNR in the 2.5 mm, 1.7 mm, and 1.1 mm datasets, respectively, when compared to standard scanner reconstructed images (p < 0.05). All whole brain, white matter, and gray matter average values at each resolution can be found in Table 2, with the final OSS-SNR achieved at each resolution as 60.3 ± 26.3 , 44.8 ± 19.1 , and 16.3 ± 5.1 at 2.5 mm, 1.7 mm, and 1.1 mm isotropic resolutions respectively, and 60.7 ± 17.5 at 2.5 mm isotropic resolution at 3T. Consistent with the prior literature, average shear stiffness is significantly greater in white matter than gray matter at all resolutions (p < 0.001, Table 2), with the average values at 1.1 mm isotropic resolution as 2.85 ± 0.19 kPa for white matter and 2.70 ± 0.19 kPa for gray matter.

We have also included a comparison of shear stiffness and damping ratio in the left and right hemispheres to access the possible asymmetry in MRE measures. This showed that when averaged over all subjects there is only a 0.4%, 0.5%, and 1.8% difference between the right and left hemispheres at 1.1 mm, 1.7 mm, and 2.5 mm isotropic resolution at 7T, respectively. The average absolute value percent difference in shear stiffness between the hemispheres is 6.4±3.2%, 7.2±3.9%, and 9.1±7.2% (Table 3) at 1.1 mm, 1.7 mm, and 2.5 mm isotropic resolution at 7T, respectively, although there are no statistically significant differences between the left and right hemisphere average stiffnesses when tested with a paired t-test (p>0.05). The average absolute value percent difference in shear stiffness between the hemispheres measured at 2.5 mm isotropic resolution on 3T MRI was 6.1±4.4% (Table 3), and there is also no statistically significant difference between the left and right hemisphere average stiffness when tested with a paired t-test (p>0.05).

We also acquired partial brain coverage 7T MRE data with 0.8 mm isotropic resolution, the first sub-millimeter human MRE reported, on three subjects from this previously described cohort to access the feasibility of submillimeter MRE. The results showed an acceptable average OSS-SNR of 12.9±0.9, with estimated average shear stiffness of 2.89±0.22 kPa, damping ratio of 0.26±0.01, gray matter shear stiffness of 2.79±0.13 kPa, and white matter shear stiffness of 3.00±0.29 kPa. Though the application of submillimeter MRE for the whole brain might be challenging for the patient's comfort due to the long total acquisition time, it might be beneficial for the focused biomechanical analysis of smaller brain regions, such as hippocampal subfields, which does not require whole brain acquisition.

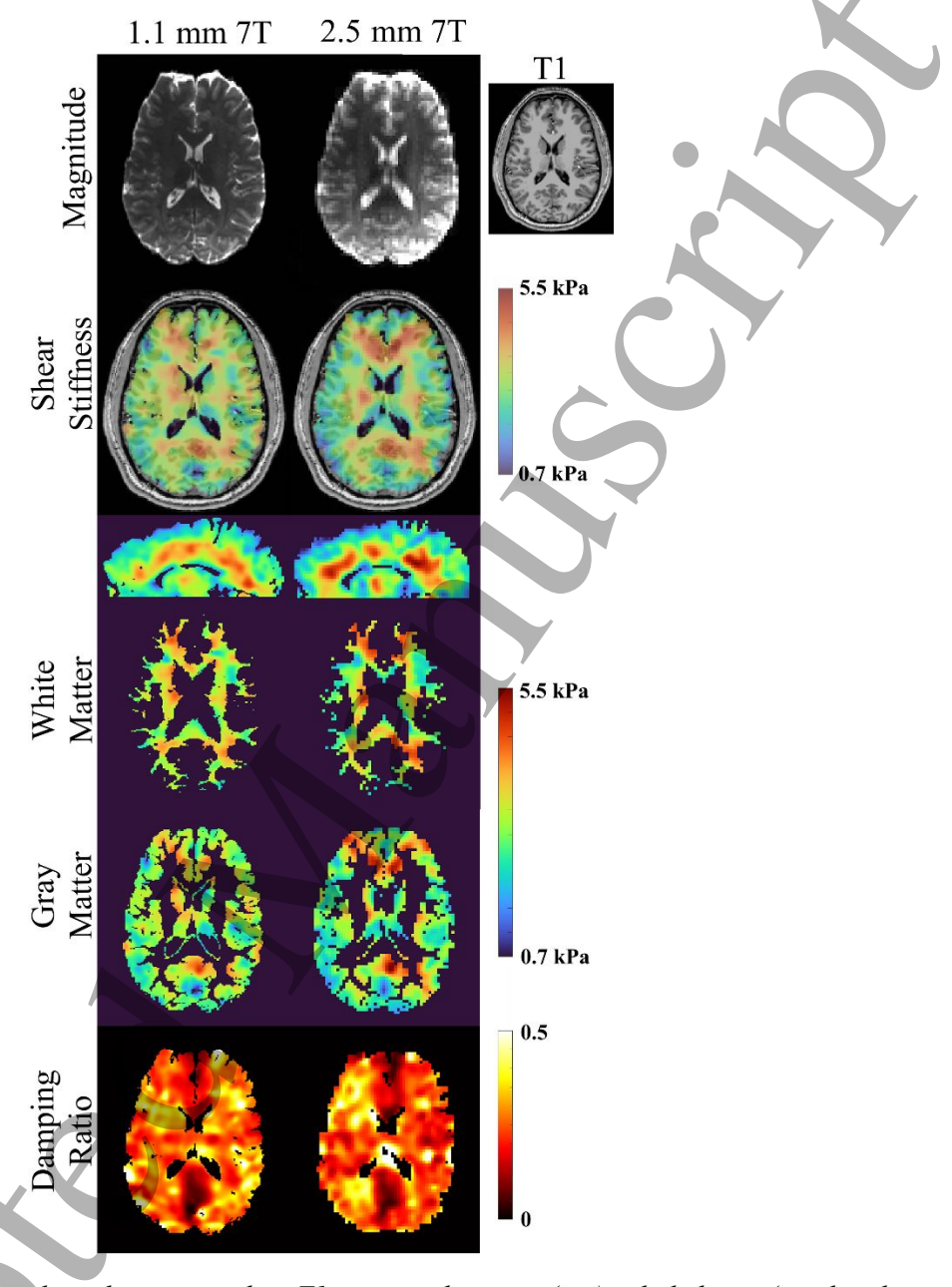


Figure 4. MRE magnitude and corresponding T1 structural images (top), whole brain (axial and sagittal), white matter, and gray matter shear stiffness maps, and damping ratio maps in one healthy human subject in the same slice for each resolution. The mean and standard deviation of the white matter shear stiffness for this subject is 2.64±0.08kPa, and the associated damping ratio is 0.25±0.01.

We observed no statistically significant difference in whole brain average shear stiffness between the 3T and 7T matched resolution datasets, as well as no significant difference in between any of the resolution groups at 7T (Table 2). An SSIM analysis on the matched resolution datasets resulted in an average score of 0.873±0.058 revealing that the results were similar, but not identical (Figure 5). This is

also exemplified by the subject-wise average percent difference between shear stiffness and damping ratio at 3T and any resolution at 7T (Table 3). We observe an average of 8.8-12.7%, 7.9-13.0%, and 8.6-13.1% percent differences in shear stiffness between the 2.5 mm resolution 3T acquisition and the 7T acquisitions in the whole brain, white matter, and gray matter, respectively (Table 3).

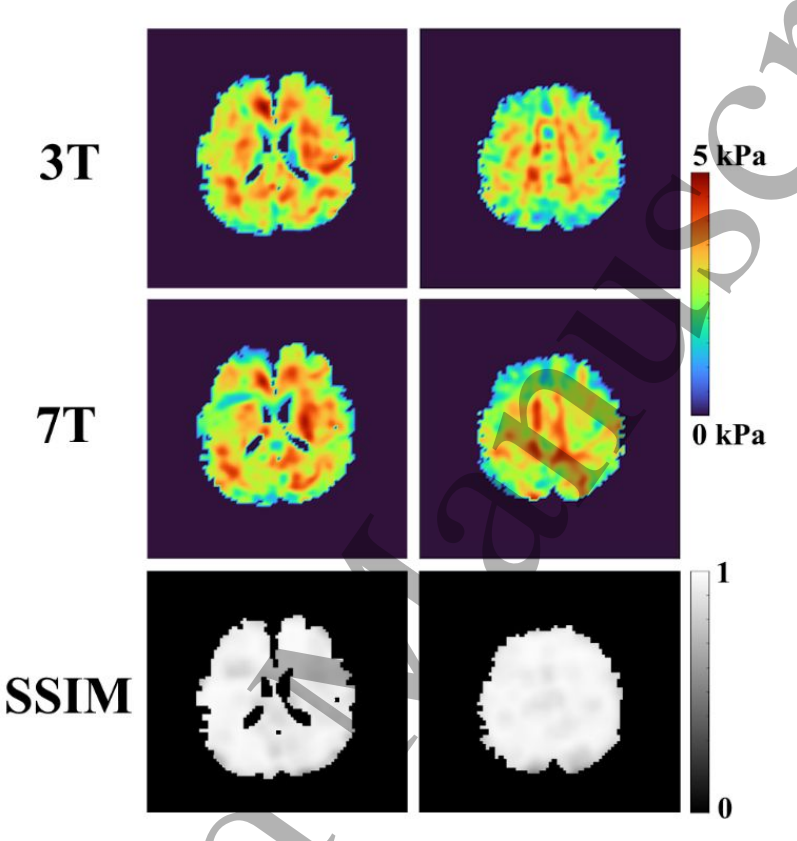


Figure 5. Elastograms and SSIM analysis on two representative slices on the same subject at 2.5 mm isotropic resolution at both 3T and 7T

As all groups are above the acceptable OSS-SNR limit (> 3) [72], we see no dependence of SNR and shear stiffness. From our repeatability analysis (one person scanned three times over the course of one week), we have a coefficient of variation of 1.88%, 9.24%, and 5.78% in the 1.1 mm, 1.7 mm, and 2.5 mm resolution groups, respectively, for shear stiffness. For the two scans performed on the same day approximately 2 hours apart, the coefficient of variation for shear stiffness across all resolutions was 3.30%. Over all the scanning sessions and resolutions, we have a coefficient of variation of 6.48% for shear stiffness.

Table 2. Whole Brain, White Matter, and Gray Matter Averages for Each Resolution with Advanced Reconstruction and Denoising Applied Concurrently (Average \pm Standard Deviation, *16 subjects only). P-values calculated from repeated measures ANOVAs between 7T resolution groups (with Bonferroni correction, significance level of p<0.017).

Whole Brain					7
Resolution	2.5 mm	1.7 mm	1.1 mm	2.5 mm (3T)*	p-value
Shear stiffness (kPa)	2.68±0.26	2.62±0.16	2.73±0.19	2.52±0.20	0.056
Damping ratio	0.25±0.03	0.26±0.02	0.27±0.03	0.25±0.03	0.004
OSS-SNR	63.5±25.8	43.4±19.3	16.5±5.3	60.7±17.5	< 0.001
White Matter					
Shear stiffness (kPa)	2.76±0.26	2.70±0.16	2.84±0.19	2.58±0.21	0.016
Damping ratio	0.25±0.02	0.26±0.02	0.27±0.03	0.25±0.03	0.015
Gray Matter					
Shear stiffness (kPa)	2.63±0.25	2.56±0.16	2.70±0.19	2.48±0.20	0.038
Damping ratio	0.25±0.03	0.27±0.02	0.27±0.03	0.25±0.03	0.005
Percent Difference Between Gray and White Matter					
Shear stiffness	4.72±2.10%	5.52±1.88%	5.40±1.57%	4.08±1.37%	=
Percent Difference Between Left and Right Hemisphere					
Shear stiffness	9.14±7.28%	7.20±3.95%	6.43±3.17%	6.07±4.41%	=
Damping Ratio	6.97±4.62%	6.17±3.87%	6.90±4.63%	8.34±7.28%	_
					_

Table 3. 7T Whole Brain, White Matter, and Gray Matter Average Percent Difference from 2.5mm Resolution 3T for Each Resolution (Average \pm Standard Deviation, 16 subjects only)

Whole Brain			
Resolution	2.5 mm	1.7 mm	1.1 mm
Shear stiffness	10.7±8.7%	8.8±5.7%	12.7±6.6%
Damping ratio	8.3±7.9%	9.5±6.8%	10.3±6.4%
White Matter			
Shear stiffness	10.4±9.2%	7.9±6.5%	13.0±6.8%
Damping ratio	7.4±7.1%	8.6±6.7%	9.2±6.2%
Gray Matter			
Shear stiffness	10.8±8.6%	8.6±5.6%	13.1±7.5%
Damping ratio	8.5±7.8%	9.4±6.3%	10.0±6.1%

Small Structures

Due to technical limitations of our 3T MRE sequence, we were unable to capture images at 1.1 mm isotropic resolution at 3T. Attempting to decrease the voxel size by that amount increased the TE and scan time greatly, and required significant sequence acceleration, increasing noise to an unacceptable level. In

addition to the resolution that one is able to achieve, we believe that one of the main benefits of implementing MRE at 7T is the resulting ability to pair it with other high resolution 7T sequences such as DTI, high resolution structural scans, or SWI.

We have here, included a stiffness comparison and stiffness contrast analysis between anatomical structures (Tables 4 & 5). Running a repeated-measures ANOVA between resolutions for each anatomical structure and global white matter, there is a significant difference (p<0.017) between resolutions in shear stiffness for each of structures shown apart from the corpus callosum and putamen, as well as between the structures shown and global white matter. There is, however, no significant difference in damping ratio between resolutions for each of the structures shown apart from the corpus callosum. It should be noted that the standard deviations in these homogenous small structures are lower at the higher resolution, implying that we see less variation in these regions likely due to partial volume effects. We also observe this in our earlier phantom experiments, where the standard deviation in shear stiffness in the stiff spherical inclusion is less at 1.1 mm isotropic resolution (0.07 kPa) than at 2.5 mm isotropic resolution (0.24 kPa).

Table 4. Average shear stiffness and damping ratio at low and high resolution of 7T MRE performed in a selection of small anatomical structures. P-values calculated from repeated measures ANOVAs between each group (with Bonferroni correction, significance level of p<0.017)

Shear Stiffness (kPa)						
Resolution	2.5 mm* (3T)	2.5 mm	1.1 mm	p-value		
Caudate	2.73±0.33	3.18±0.47	3.37±0.43	< 0.001		
Corpus Callosum	3.01 ± 0.31	3.13 ± 0.49	3.34 ± 0.35	0.0465		
Hippocampus	2.13±0.52	2.59 ± 0.49	2.80 ± 0.48	0.0012		
Putamen	3.41 ± 0.35	3.70 ± 0.57	3.71 ± 0.35	0.1720		
Thalamus	2.68±0.42	3.34 ± 0.61	3.70 ± 0.46	< 0.001		
Damping Ratio						
Caudate	0.290±0.044	0.277±0.034	0.265±0.039	0.1085		
Corpus Callosum	0.185±0.042	0.226 ± 0.050	0.222 ± 0.031	0.0041		
Hippocampus	0.239 ± 0.046	0.224 ± 0.048	0.235 ± 0.038	0.1887		
Putamen	0.227 ± 0.051	0.242 ± 0.042	0.250 ± 0.034	0.4084		
Thalamus	0.228±0.039	0.248 ± 0.041	0.244 ± 0.027	0.1063		

Table 5. Average shear stiffness contrast between structures at low and high resolution of 7T MRE

Shear Stiffness Contrast					
Resolution	2.5 mm* (3T)	2.5 mm	1.1 mm		
Caudate vs WM	0.075±0.129	0.175±0.163	0.189±0.156		
Corpus Callosum vs WM	0.179 ± 0.098	0.144 ± 0.148	0.179±0.119		
Hippocampus vs WM	-0.145±0.225	-0.060±0.156	-0.020±0.156		
Putamen vs WM	0.339 ± 0.136	0.333 ± 0.155	0.297±0.117		
Thalamus vs WM	0.055±0.159	0.216±0.131	0.291±0.141		
Caudate vs GM	0.146 ± 0.146	0.235±0.186	0.267±0.175		
Corpus Callosum vs GM	0.255 ± 0.116	0.202±0.161	0.256±0.140		
Hippocampus vs GM	-0.095±0.231	-0.012±0.169	0.043±0.163		
Putamen vs GM	0.425 ± 0.158	0.400±0.171	0.381 ± 0.126		
Thalamus vs GM	0.124 ± 0.181	0.278±0.153	0.375±0.154		
Caudate vs Putamen	0.261±0.178	0.146±0.133	0.108±0.092		

Discussion

In this work, MRE was successfully implemented at multiple resolutions at 7T using a custom pneumatic actuator and motion sensitive single-shot EPI-based sequence, with advanced post-processing and nonlinear inversion algorithm to calculate the mechanical properties of the brain and its substructures at high resolution. The development and use of sub-millimeter MRE, or high resolution MRE such as 1.1 mm, on the human brain or other tissues will require the use of 7T due to technical limitations at lower field strengths. Although only discussed briefly in this paper, we have demonstrated the first sub-millimeter MRE results. While sub-millimeter MRE still requires more validation and repeatability analysis, it will be imperative for clinical applicability to diseases and disorders of the human brain that affect small regions, such as the subfields of the hippocampus. Additionally, in tissues apart from the brain where higher frequency actuation can be used, this higher resolution that can only be achieved at 7T must be used to capture enough points along the shear wavelength for a stable and accurate inversion. 7T has been shown to have significant advantages in a variety of sequence like T1, DTI, and SWI [63], [80]. These advantages have led to a substantial amount of clinical research done in this field. If MRE is to be incorporated into a 7T MRI studies, because brain stiffness and damping ratio depend on other characteristics of the human brain, it is crucial that other high resolution MRI modalities be recorded in the same scanning session as MRE. All of these modalities can be used to then contextualize the MRE result with high spatial accuracy. In order to perform an investigation into the effect of different resolutions on MRE property maps, 7T is required for acquisition of the full range of resolution. As shown in this study, 3T and 7T MRE at 2.5 mm isotropic resolutions are comparable, and not only can higher resolutions only be achieved at 7T,

consistency between scanners and sequences is important for comparison studies as shown by our higher between-scanner variation results.

In using our custom elasticity phantom, we validated the accuracy of our sequence and proposed post-processing procedures. We have confirmed that in a linearly elastic material with no known complex microstructure, there are no inherent differences when upgrading to high resolutions at 7T. Using phantom scans, we also investigated the benefits of higher resolution to resolve small structures, e.g., the spherical inclusions. While we achieved a measurement of shear stiffness within the manufacturing specifications of the softer inclusion at both 2.5 mm and 1.1 mm resolutions, a shear stiffness closer to the manufacturing specifications for the stiffer inclusion at 1.1 mm isotropic resolution was found. We hypothesize that this is due to the larger difference between the background shear modulus (1.70 kPa) and the modulus of the stiffer inclusion (2.70 kPa) compared to the softer inclusion (1.00 kPa). The higher resolution acquisition can better resolve the changes in wavelength and wave speed between materials of different mechanical properties, therefore achieving a more accurate measurement even when tissue types that are beside each other are different. This is also exemplified in Figure 3, where the edges of the spherical inclusions appear sharper at 1.1 mm resolution compared to 2.5 mm. There is, additionally, still no significant difference in apparent shear stiffness of the background shear modulus in the phantom between resolution groups despite the lower OSS-SNR, as these values were still above the recommended threshold for stable nonlinear inversion of 3.0 as determined by McGarry, et al. [72].

Although moving to higher resolution at 7T can theoretically decrease vibrational motion sensitivity, we found similar intra-subject vibrational amplitudes across all scan types, with the largest variability being inter-subject. In all resolution groups, overall, using advanced reconstruction with Gadgetron framework and applying denoising significantly increases OSS-SNR. Taking into consideration the scan duration for each resolution, phantom validation results, and average OSS-SNR after the advanced reconstruction techniques, we have established 1.1 mm isotropic resolution as the most suitable and robust for MRE at 7T to calculate the viscoelastic properties of the whole human brain. In this study, we endeavored to decrease voxel volume by a factor of ~3 at each step. Our starting point was the voxel size that we commonly use at 3T- 2.5 mm isotropic resolution (15.6 mm³ voxel size). We then decreased by a factor of 3 to 1.7 mm isotropic (5.0 mm³ voxel size), and then again by another factor of 3 to 1.1 mm isotropic resolution. 1.1 mm isotropic resolution (1.3 mm³ voxel size) was picked as the stopping point for the entire cohort due to scan time, TE length, noise levels, and to match the resolution of the 7T DTI scan that was also performed on all subjects in this cohort and is implemented in many clinical studies. While higher resolution with the current sequence and post-processing algorithm is possible (shown in this study as feasibility of 0.8 mm isotropic resolution), this would increase scan time and make the scan uncomfortable for participants and therefore more prone to motion artifacts.

Despite no group differences in whole brain average shear stiffness between the 3T and 7T matched resolution datasets, as well as no significant difference in between any of the resolution groups at 7T, the results were not identical. Specifically looking at the differences in matched resolution between 3T and 7T through the SSIM analysis, many subjects were scanned on different days, which decreases the repeatability of the result according to our repeatability analysis. We identified a same-scanner, same-day 1.5-2.5 % testretest variation, a same-scanner, different-day 5.5-7.5% test-retest variation, and a different-scanner, different-day 7-13% test-retest variation (Table 3). While our same-scanner, same-day test-retest variation is similar to that of other human brain MRE studies (ranging from 1-5%) [52], [81], [82], [83], [84], different-day test-retest analysis is rarely performed for MRE and, to our knowledge, has not been reported for human brain MRE. Currently, the only commercial application of MRE is in the detection of liver fibrosis in which the acceptable level of variation is set at 7% for commercial use for same-scanner, within-7 day test-retest analysis (via the MRE QIBA Profile) [85]. However, the scale at which liver fibrosis alters liver stiffness is much larger than any changes [86], [87] we have seen in the stiffness of brain tissue as it relates to neurological disorders like dementias or multiple sclerosis. There was, however a very recent study investigating multi-site and multi-scanner test-retest repeatability of phantom stiffness measurement using the various commercial MR Elastography devices, sequences, and software [88]. This study found a 7.0% (95% CI: 2.9, 11.2) variation using the same sequence at different sites on the same elastography phantoms, which is consistent with the differences we found in the human brain [88]. This would then indicate that our study's level of variation is considered acceptable. Based on the results from the multi-site phantom study and this study, consistency in sequence and scanner appear to be very important for consistency in data between subjects. Therefore, when proposing a clinical study investigating differences between healthy controls and a patient population, either all subjects should be scanned on the same scanner with the same protocol, or the scanner used should be included as a covariate.

Current MRE studies investigating clinical populations are comparatively small and use the same site, scanner, and protocol within each study. While we do not see as large of a difference between healthy and diseased tissue as we would in the liver, studies investigating the difference between Alzheimer's patients and healthy controls have found a 8-26% difference depending on the brain region [89]. Similar differences were found between healthy controls and patients with normal pressure hydrocephalus (11-24%) [89]. Given all these levels of change due to clinical pathologies in previous studies with similar same-day test-retest variation, we can establish that our sequence and post-processing procedure would be able to discriminate between healthy tissue and pathology, such as Alzheimer's disease or mild cognitive impairment, which we have found previously in pilot studies [60].

While it is hypothesized that brain shear stiffness represents tissue structure and damping ratio reflects tissue organization [75], [90], what these metrics wholly represent in the brain is still not fully

understood, it is clear that (with the current state of the field) we cannot use brain MRE alone to diagnose or assess clinical disorders. It is unlikely that the use of brain MRE alone will be used in the future to diagnose an individual based on a quantitative stiffness range that is available for the liver due to intersubject variability based on age, sex, and other characteristics. This result implies that brain stiffness may change throughout the day, similar to other physiological phenomena that are observable through MRI. For example, cerebral blood flow velocity has a daily rhythm, where it is lower in the morning than the afternoon or evening, and is hypothesized to be related with sleep-associated processes [91]. As prior investigations have shown correlations between cerebral blood flow and shear stiffness [92], this may influence our results. Alternatively, subject hydration, intracranial pressure, amount of sleep, or even recent performance of high intensity exercise [91], [92], [93], [94], [95], [96] also contribute to daily fluctuations in brain shear stiffness, and these factors have been shown to have effects on the results of other MRI sequences such as BOLD or fMRI [97], [98], [99], [100]. This is also a related advantage of using 7T MRE, as 7T offers high resolution scans of other features of the human brain (like perfusion or white matter integrity) [63], [80], [101], which can be then used to contextualize the information we gather through using MRE. These other features, along with others like age or sex, should therefore be used as covariates in analyses using MRE in clinical assessment in pertinent diseases and when trying to discriminate between healthy controls and clinical patients.

There is currently no known ground truth for how the different small anatomical structures of the caudate, hippocampus, putamen, and thalamus differ from each other in stiffness, or what the contrast should be between these features, and we can therefore not confirm the accuracy of these contrast differences. However, using the same nonlinear inversion scheme, a previous phantom study determined that inclusions as small as 8 mm and stiffness contrast as low as 14% could be detected using 2 mm isotropic resolution [41]. In the human brain, analyzing the average stiffnesses using a different resolution (1.6 mm isotropic resolution), but the same nonlinear inversion algorithm at 3T from prior investigations, we see a comparable value of the shear stiffness of the caudate (3.75 kPa), putamen (3.87 kPa), and thalamus (3.82 kPa), but a lower value in the hippocampus (3.35 kPa) [82]. However, the shear stiffness in the hippocampus is similar to more recent studies with similar protocols and post-processing pipelines (μ = 2.86 kPa or μ = 2.97 kPa) [102], [103]. We also observe a similar inter-subject variance and bilateral symmetry [82], [102], [103].

Unlike previous investigations [25], [33], [43], [45], [46], [47], [48], [50], [104], we saw no statistically significant difference between whole brain shear stiffness between resolution groups despite the results not being identical. The trend of decreased apparent stiffness values with increasing resolution when employing a direct inversion method was also specifically identified by Barnhill, *et al.* [45] and Marshall, *et al.* [46] in the same subject populations, who hypothesized that a different distribution of

features is being captured at high-resolution [45]. It was further hypothesized that higher resolution scans, which capture fine features and interfaces not visible at low resolution, produce lower elasticity estimates due to these finer features creating more tortuosity in the wave [45], [48]. Neither of these studies, however, investigated the effect of SNR, post-processing techniques, or inversion method, nor did they investigate matched resolution scans between field strengths, so the lack of controlled variables made it difficult to support this hypothesis further. The difference in our findings can be attributed to a variety of factors. For example, by acquiring data at multiple resolutions, including matching the 3T acquisition resolution, we remove any bias that up-sampling or down-sampling may introduce. Also, by ensuring that each individual's OSS-SNR were above the stability threshold of 3.0 and that all acquisitions had a similar vibrational amplitude range, we maximize data quality for inversion processing. This investigation is the first to utilize nonlinear inversion on 7T data, and is the first to investigate the difference between 3T and 7T using such an algorithm, so this is likely a large contributing factor.

Due to the finite element (FE) nature of the nonlinear inversion algorithm used in this investigation, the resolution of MRE is not governed by the wavelength of the shear wave as it is in direct inversion methods such as local frequency estimation [105], [106]. This is likely why this investigation, and others that use nonlinear inversion, find little to no relationship between imaging resolution and whole-brain mechanical property values [8], while investigations such as Barnhill, *et al.* and Marshall, *et al.* [45], [46] that utilized methods that rely on local spatial frequency do find this relationship. Due to this FE nature of nonlinear inversion removing the reliance of resolution on shear wave wavelength, nonlinear inversion can be used to characterize the mechanical behavior of brain tissue using intrinsic actuation of ~1-3 Hz [55], [107], [108].

However, it is worth mentioning that nonlinear inversion is somewhat governed by the FE parameters used. In the past, nonlinear inversion subzone parameter variations and their influence on the reconstructed mechanical parameters has been studied [40], [41]. This study concluded that the stable subzone range for accurate and repeatable inversion was between $0.64L_s$ and $1.0L_s$ in the human brain, where L_s is the shear wavelength in the tissue given the frequency of actuation. In the human brain at 50 Hz, L_s = 30.6 mm. Therefore, in this investigation we use a subzone size of 19.6 mm. It has also previously been established [42] by investigating multi-resolution meshes that eight nodes per wavelength in the FE mesh is sufficient in phantoms for accurate mechanical property recovery, but that mechanical property estimation from 50 Hz *in vivo* brain data stabilizes once the displacement resolution reaches 1.7 mm, or around 19 nodes per wavelength. At our highest imaging resolution of 1.1 mm, this gives around 27 nodes per wavelength. While a full investigation into how data resolution and acquisition frequency affect the achievable resolution for nonlinear inversion should be performed in the future (as has been noted in previous papers investigating nonlinear inversion, such as Solamen, *et al.*) [41], this would require

extensive FE simulation and is beyond the scope of this investigation.

Advanced processing techniques such as rigid body motion correction to phase images, B_0 correction, and distortion corrections are not incorporated into the proposed framework but may be considered in the future. Rigid body motion correction is partly addressed in the current framework by removing the 0 Hz component of motion during the Fourier decomposition step and EDDY-QC correction to MRE magnitude images, although a prior investigation utilized an SPM-based realign routine, resulting in sharper looking images [47]. As stated earlier, we also employed a 4th order low-pass spatial filter to remove a high-frequency 'z-striping' effect that occurs when there is slight volunteer rigid-body motion between the odd and even slice acquisitions during our interleaved acquisition structure. In the case where this occurs, the nonlinear inversion algorithm optimization solution will diverge due to the artificial highfrequency wavelength. While this low pass filter may marginally affect the apparent resolution in the zdirection, it should not cause blurring such as with a generally applied gaussian or median filter, as it is only intended to remove high-frequency spatial wavelengths. In the future, the necessity of this low-pass filter may be avoided by using a different encoding structure, such as spiral acquisition which has been successfully used in various 3T sequences [36]. In MRE with EPI readout, typically, B₀ and geometric distortion correction are interrelated, as B₀ inhomogeneities result in said geometric distortions[47]. This technique, however, requires either an additional Bo field map at the time of data collection or additional acquisition with reversed encoding directions [47], [109], and while this correction appears quite significant in simulations, its effect is less so in vivo [109]. While Gadgetron has a functionality to perform B₀ correction without such a field map, this algorithm has not been applied. Generally, the potential corrections were not implemented at this time, as to not introduce additional controlled bias, as they have not been shown to be accurate in correction of average stiffness values [109]. Additionally, other recently developed advanced methods could benefit the pipeline in the future, such as AI-based unwrapping and inversion [110], radial sampling and undersampling [111], an MRE actuator that would benefit from the 7T static field strength (such as electromagnetic-coil-based actuator) [112], or a different inversion scheme that would consider tissue fluidity or tractography [113], [114].

Additionally, one potential drawback of using a denoising technique is the possibility of an artificially increased OSS-SNR due to the general removal of higher order components [83], [115]. This effect has been observed when using filtering such as Gaussian or Median filtering [48], [53], [54], [55], [56], [57], [58], [83], which also result in the blurring of fine physiological features. However, the MP-PCA method aims to remove only the noise without interfering with the signal itself (*i.e.*, without blurring features) [59]. The denoising algorithm is additionally applied in local patches without assumptions on noise levels. Therefore, under the assumption smoothly varying noise maps (*i.e.*, noise being constant within a local patch), the denoising can be used on data with spatially varying noise levels [115] and

estimate such noise maps accordingly [116]. Just like smoothing, the MP-PCA will not correct the signal offset due to non-Gaussian MR signals, as the algorithm removes random signal fluctuations without interfering with the signal [59], [116]. Therefore, the average signal is not altered. If the data are non-Gaussian distributed (*e.g.*, Rician), then the noise will be removed, but the Rician noise floor will be preserved.

Conclusion

In conclusion, we have demonstrated the repeatability and robustness of high-resolution whole brain 7T MRE with an advanced post-processing pipeline and nonlinear viscoelastic inversion. Capturing finer viscoelastic features with higher imaging resolutions can be investigated further in future studies by utilizing heterogeneous phantoms with known mechanical properties and by analyzing differences in smaller brain regions, which is one of the goals of using such high-resolution scans. The developed techniques will be used in future studies to investigate biomechanical parameters of small volume brain sub-structures with applications in neurodegenerative diseases and other relevant neurological disorders.



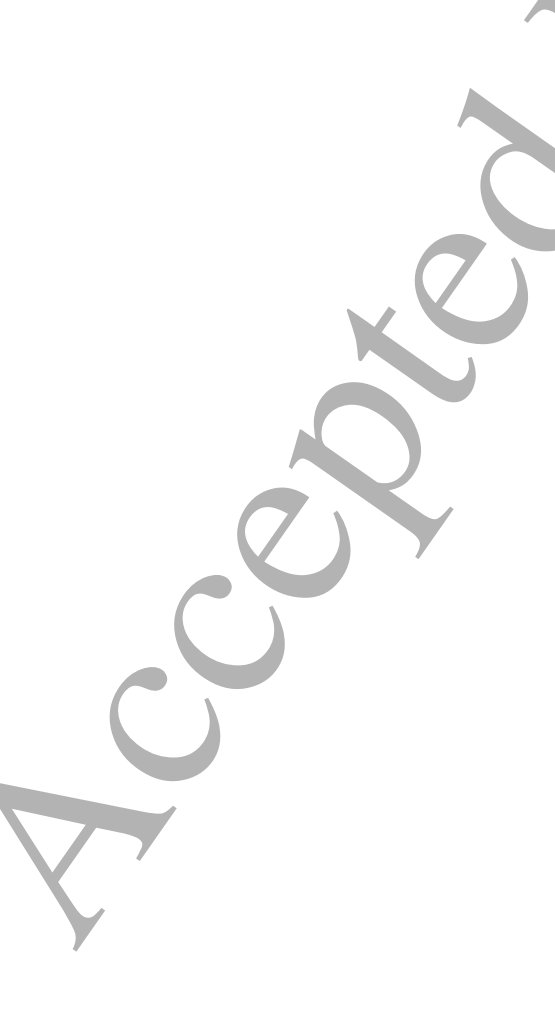
Data and Code Availability: The MP-PCA denoising code can be found on the GitHub page NYU-DiffusionMRI/mppca_denoise. Gadgetron is an open-source framework.

Funding: This work was supported by R01EB027075, NSF CMMI 1953323, and NIH R21AG071179.

Declaration of Competing Interests: J. Veraart is co-inventor of a patent (US20180120404Å1) that relates to technology used in this study. Priti Balchandani is a named inventor on patents relating to magnetic resonance imaging (MRI) and RF pulse design. The patents have been licensed to GE Healthcare, Siemens AG, and Philips international.

Acknowledgements: The authors would like to thank Ms. Aislinn Diaz for assistance in volunteer recruitment and coordination, and Dr. Curtis Johnson for technical support with the 3T MRE sequence.

Ethics Statement: This study's activities were approved by the Institutional Review Board at the Icahn School of Medicine at Mount Sinai Hospital (STUDY-14-00404). This research is in accordance with the principles embodied in the Declaration of Helsinki, and all participants gave written informed consent to participate in the study.



References

- [1] R. Muthupillai, P. J. Rossman, D. J. Lomas, J. F. Greenleaf, S. J. Riederer, and R. L. Ehman, "Magnetic resonance imaging of transverse acoustic strain waves," *Magn Reson Med*, vol. 36, no. 2, pp. 266–274, 1996.
- [2] E. H. Clayton, G. M. Genin, and P. V. Bayly, "Transmission, attenuation and reflection of shear waves in the human brain," *J R Soc Interface*, vol. 9, no. 76, pp. 2899–2910, 2012, doi: 10.1098/rsif.2012.0325.
- [3] Z. T. H. Tse, H. Janssen, A. Hamed, M. Ristic, I. Young, and M. Lamperth, "Magnetic resonance elastography hardware design: A survey," *Proc Inst Mech Eng H*, vol. 223, no. 4, pp. 497–514, 2009, doi: 10.1243/09544119JEIM529.
- [4] J. Guo *et al.*, "Towards an Elastographic Atlas of Brain Anatomy," *PLoS One*, vol. 8, no. 8, 2013, doi: 10.1371/journal.pone.0071807.
- [5] C. L. Johnson *et al.*, "MR elastography of intercranial tumors: initial experience with high-resolution imaging and nonlinear inversion," in *ISMRM 2016*, 2016. doi: 10.1007/s00062-014-0311-9.
- [6] J. Zhang, M. A. Green, R. Sinkus, and L. E. Bilston, "Viscoelastic properties of human cerebellum using magnetic resonance elastography," *J Biomech*, vol. 44, no. 10, pp. 1909–1913, 2011, doi: 10.1016/j.jbiomech.2011.04.034.
- [7] M. Kurt *et al.*, "Optimization of a Multifrequency Magnetic Resonance Elastography Protocol for the Human Brain," *Journal of Neuroimaging*, vol. 29, no. 4, pp. 440–446, 2019, doi: 10.1111/jon.12619.
- [8] L. V. Hiscox *et al.*, "Standard-space atlas of the viscoelastic properties of the human brain," *Hum Brain Mapp*, vol. 41, no. 18, pp. 5282–5300, 2020, doi: 10.1002/hbm.25192.
- [9] J. Huston *et al.*, "Magnetic resonance elastography of frontotemporal dementia," *Journal of Magnetic Resonance Imaging*, vol. 43, no. 2, pp. 474–478, 2016, doi: 10.1002/jmri.24977.
- [10] M. C. Murphy *et al.*, "Regional brain stiffness changes across the Alzheimer's disease spectrum," *Neuroimage Clin*, vol. 10, pp. 283–290, 2016, doi: 10.1016/j.nicl.2015.12.007.
- [11] K. J. Streitberger *et al.*, "In vivo viscoelastic properties of the brain in normal pressure hydrocephalus," *NMR Biomed*, vol. 24, no. 4, pp. 385–392, 2011, doi: 10.1002/nbm.1602.
- [12] J. Huston, A. Perry, N. Fattahi, A. Arani, F. Meyer, and R. Ehman, "Magnetic resonance elastography demonstrates increased brain stiffness in normal pressure hydrocephalus," *Fluids Barriers CNS*, vol. 12, no. Suppl 1, p. O38, 2015, doi: 10.1007/978-1-4939-1575-0.
- [13] A. Perry *et al.*, "Clinical Correlation of Abnormal Findings on Magnetic Resonance Elastography in Idiopathic Normal Pressure Hydrocephalus," *World Neurosurg*, vol. 99, pp. 695–700, 2017, doi: 10.1016/j.wneu.2016.12.121.

- [14] A. J. Pattison, S. S. Lollis, P. R. Perrinez, J. B. Weaver, and K. D. Paulsen, "MR elastography of hydrocephalus," in *Proceedings of SPIE The International Society for Optical Engineering*, 2009, pp. 72620A0-8. doi: 10.1117/12.811820.
- [15] G. McIlvain, H. Schwarb, N. J. Cohen, E. H. Telzer, and C. L. Johnson, "Mechanical properties of the in vivo adolescent human brain," *Dev Cogn Neurosci*, vol. 34, pp. 27–33, 2018, doi: 10.1016/j.dcn.2018.06.001.
- [16] I. Sack *et al.*, "The impact of aging and gender on brain viscoelasticity," *Neuroimage*, vol. 46, no. 3, pp. 652–657, 2009, doi: 10.1016/j.neuroimage.2009.02.040.
- [17] L. V. Hiscox *et al.*, "High-reolution magnetic resonance elastogrohy reveals differences in subcortical gray matter viscoelasticity between young and healthy older adults," *Neurobiol Aging*, vol. 65, pp. 158–167, 2018.
- [18] I. Sack, K. J. Streitberger, D. Krefting, F. Paul, and J. Braun, "The influence of physiological aging and atrophy on brain viscoelastic properties in humans," *PLoS One*, vol. 6, no. 9, 2011, doi: 10.1371/journal.pone.0023451.
- [19] A. Fehlner, J. Guo, K. J. Streitberger, S. Hirsch, J. Braun, and I. Sack, "The viscoelastic response of the human brain to functional activation detected by magnetic resonance elastography," in *Proceedings of the 22nd Annul Meeting of ISMRM, Milan*, 2014.
- [20] Y. C. Chuang *et al.*, "Myelination dictates axonal viscoelasticity," *European Journal of Neuroscience*, vol. 57, no. 8, 2023, doi: 10.1111/ejn.15954.
- [21] J. Wuerfel *et al.*, "MR-elastography reveals degradation of tissue integrity in multiple sclerosis," *Neuroimage*, vol. 49, no. 3, pp. 2520–2525, 2010, doi: 10.1016/j.neuroimage.2009.06.018.
- [22] C. L. Johnson *et al.*, "Multiple sclerosis lesions are softer than surrounding white matter : An MR elastography study," in *ISMRM 2017 Conference Proceedings*, 2017.
- [23] K. J. Streitberger *et al.*, "Brain viscoelasticity alteration in chronic-progressive multiple sclerosis," *PLoS One*, vol. 7, no. 1, 2012, doi: 10.1371/journal.pone.0029888.
- [24] A. Lipp *et al.*, "Cerebral magnetic resonance elastography in supranuclear palsy and idiopathic Parkinson's disease," *Neuroimage Clin*, vol. 3, pp. 381–387, 2013, doi: 10.1016/j.nicl.2013.09.006.
- [25] A. Lipp, C. Skowronek, A. Fehlner, K. J. Streitberger, J. Braun, and I. Sack, "Progressive supranuclear palsy and idiopathic Parkinson's disease are associated with local reduction of in vivo brain viscoelasticity," *Eur Radiol*, vol. 28, no. 8, pp. 3347–3354, 2018, doi: 10.1007/s00330-017-5269-y.
- [26] M. C. Murphy *et al.*, "Decreased brain stiffness in alzheimer's disease determined by magnetic resonance elastography," *Journal of Magnetic Resonance Imaging*, vol. 34, pp. 494–498, 2011.
- [27] L. V Hiscox *et al.*, "Mechanical property alterations across the cerebral cortex due to Alzheimer's disease," *Brain Commun*, vol. 2, no. 1, 2019, doi: 10.1093/braincomms/fcz049.

- [28] M. M. ElSheikh *et al.*, "MR elastography demonstrates unique regional brain stiffness patterns in dementias," *AJR Am J Roentgenol*, vol. 209, no. 2, pp. 403–408, 2017, doi: 10.2214/AJR.16.17455.MR.
- [29] L. M. Gerischer, A. Fehlner, T. Köbe, J. Braun, I. Sack, and F. Agnes, "High resolution MR elastography of the hippocampus as a novel biomarker for Alzheimer's disease?," in *Clinical Neurophysiology*, 2016, pp. e216–e217. doi: 10.1016/j.clinph.2016.05.029.
- [30] E. Ozkaya *et al.*, "Viscoelasticity of children and adolescent brains through MR elastography," *J Mech Behav Biomed Mater*, vol. 115, no. December 2020, p. 104229, 2021, doi: 10.1016/j.jmbbm.2020.104229.
- [31] E. Barnhill *et al.*, "Nonlinear multiscale regularisation in MR elastography: Towards fine feature mapping," *Med Image Anal*, vol. 35, pp. 133–145, 2017, doi: 10.1016/j.media.2016.05.012.
- [32] M. A. Green, L. E. Bilston, and R. Sinkus, "In vivo brain viscoelastic properties measured by magnetic resonance elastography," *NMR Biomed*, vol. 21, no. 4, pp. 448–467, 2008, doi: 10.1002/nbm.
- [33] U. Hamhaber, I. Sack, S. Papazoglou, J. Rump, D. Klatt, and J. Braun, "Three-dimensional analysis of shear wave propagation observed by in vivo magnetic resonance elastography of the brain," *Acta Biomater*, vol. 3, no. 1, pp. 127–137, 2007, doi: 10.1016/j.actbio.2006.08.007.
- [34] U. Hamhaber *et al.*, "In vivo magnetic resonance elastography of human brain at 7 T and 1.5 T," *Journal of Magnetic Resonance Imaging*, vol. 32, no. 3, pp. 577–583, 2010, doi: 10.1002/jmri.22294.
- [35] C. L. Johnson *et al.*, "Local mechanical properties of white matter structures in the human brain," *Neuroimage*, no. 79, pp. 145–152, 2013, doi: 10.1016/j.neuroimage.2013.04.089.Local.
- [36] C. L. Johnson *et al.*, "Magnetic resonance elastography of the brain using multi-shot spiral readouts with self-navigated motion correction," *Magn Reson Med*, vol. 70, no. 2, pp. 404–412, 2013, doi: 10.1038/jid.2014.371.
- [37] E. Ozkaya *et al.*, "Brain-mimicking phantom for biomechanical validation of motion sensitive MR imaging techniques," *J Mech Behav Biomed Mater*, vol. 122, p. 104680, 2021, doi: https://doi.org/10.1016/j.jmbbm.2021.104680.
- [38] H. Lv *et al.*, "MR elastography frequency–dependent and independent parameters demonstrate accelerated decrease of brain stiffness in elder subjects," *Eur Radiol*, vol. 30, no. 12, pp. 6614–6623, Dec. 2020, doi: 10.1007/s00330-020-07054-7.
- [39] J. T. Vaughan *et al.*, "7T vs. 4T: RF power, homogeneity, and signal-to-noise comparison in head images," *Magn Reson Med*, vol. 46, no. 1, pp. 24–30, 2001, doi: 10.1002/mrm.1156.
- [40] A. T. Anderson *et al.*, "Inversion Parameters based on Convergence and Error Metrics for Nonlinear Inversion MR Elastography," in *ISMRM & ISMRT Annual Meeting and Exhibition 2017*, 2017. [Online]. Available: https://cds.ismrm.org/protected/17MProceedings/PDFfiles/1139.html

- [41] L. M. Solamen, M. D. McGarry, L. Tan, J. B. Weaver, and K. D. Paulsen, "Phantom evaluations of nonlinear inversion MR elastography," *Phys Med Biol*, vol. 63, no. 14, 2018, doi: 10.1088/1361-6560/aacb08.
- [42] M. D. J. McGarry *et al.*, "Multiresolution MR elastography using nonlinear inversion," *Med Phys*, vol. 39, no. 10, pp. 6388–6396, 2012, doi: 10.1118/1.4754649.
- [43] J. Braun *et al.*, "High-resolution mechanical imaging of the human brain by three-dimensional multifrequency magnetic resonance elastography at 7T," *Neuroimage*, vol. 90, pp. 308–314, 2014, doi: 10.1016/j.neuroimage.2013.12.032.
- [44] L. V Hiscox *et al.*, "Magnetic resonance elastography (mre) of the human brain: technique, findings and clinical applications," *Phys Med Biol*, vol. 61, no. 24, p. R401, 2016.
- [45] E. Barnhill *et al.*, "Impact of Field Strength and Image Resolution on MRE Stiffness Estimation," in *Proc 24th Annual Meeting ISMRM*, 2016.
- [46] H. Marshall *et al.*, "Magnetic resonance elastography (MRE) reproducibility study in the same participants at field strengths of 1.5, 3, and 7 Tesla," in *First International MRE Workshop in Berlin*, 2017, p. 25. [Online]. Available: https://elastography.de/wp-content/uploads/2017/03/ABSTRACT-BOOK_FINAL_NEU.pdf
- [47] A. Fehlner *et al.*, "Increasing the spatial resolution and sensitivity of magnetic resonance elastography by correcting for subject motion and susceptibility-induced image distortions," *Journal of Magnetic Resonance Imaging*, vol. 46, no. 1, pp. 134–141, 2017, doi: 10.1002/jmri.25516.
- [48] E. Barnhill, F. Dittmann, S. Hirsch, J. Guo, J. Braun, and I. Sack, "Investigation Of The Relationship Between Feature Detail And Stiffness Estimate In Magnetic Resonance Elastography (MRE) Elastograms," *Proc 24th Annual Meeting ISMRM*, pp. 22–24, 2016.
- [49] E. R. Triolo, O. Khegai, A. Alipour, P. Kennedy, P. Balchandani, and M. Kurt, "Validation and testing of 7T MR elastography sequence and stiffness reconstruction," in *BMES 2021*, 2021.
- [50] E. Triolo *et al.*, "Parameter Optimization for High-Resolution MR Elastography of the Human Brain at 7T," in *Proc. ISMRM-ESMRMB 31st Annual Meeting*, 2022.
- [51] E. Triolo *et al.*, "Development and validation of an ultra-high field compatible MR elastography actuator," in *Summer Biomechanics, Bioengineering and Biotransport Conference*, 2021, p. SB3C2021-325.
- [52] M. C. Murphy *et al.*, "Measuring the characteristic topography of brain stiffness with magnetic resonance elastography," *PLoS One*, vol. 8, no. 12, pp. 1–14, 2013, doi: 10.1371/journal.pone.0081668.
- [53] E. Barnhill, I. Selesnick, I. Sack, J. Braun, and N. Roberts, "Impact of Wavelet Thresholding Methods on MR Elastography Human Brain Stiffness Results," 2014.
- [54] G. Mcilvain, A. J. Hannum, A. G. Christodoulou, M. D. J. Mcgarry, and C. L. Johnson, "Low-Rank Denoising of Magnetic Resonance Elastography Images," *ISMRM Conference Proceedings*, 2019.

- [55] L. M. Solamen, S. W. Gordon-Wylie, M. D. McGarry, J. B. Weaver, and K. D. Paulsen, "Phantom evaluations of low frequency MR elastography," *Phys Med Biol*, vol. 64, no. 6, pp. 0–14, 2019, doi: 10.1088/1361-6560/ab0290.
- [56] A. Manduca, D. S. Lake, and R. L. Ehman, "Spatio-temporal Directional Filtering for Improved Inversion of MR Elastography Images," in *MICCAI 2002, LNCS 2489*, 2002, pp. 293–299.
- [57] A. Manduca, D. S. Lake, and R. L. Ehman, "Improved inversion of MR elastography images by spatio-temporal directional filtering," *Medical Imaging 2003: Image Processing*, vol. 5032, no. May 2003, p. 445, 2003, doi: 10.1117/12.483589.
- [58] B. N. Li *et al.*, "Evaluation of robust wave image processing methods for magnetic resonance elastography," *Comput Biol Med*, vol. 54, pp. 100–108, 2014, doi: 10.1016/j.compbiomed.2014.08.024.
- [59] J. Veraart, D. S. Novikov, D. Christiaens, B. Ades-aron, J. Sijbers, and E. Fieremans, "Denoising of diffusion MRI using random matrix theory," *Neuroimage*, vol. 142, pp. 394–406, 2016, doi: 10.1016/j.neuroimage.2016.08.016.
- [60] E. Triolo, O. Khegai, A. Alipour, T. Hedden, P. Balchandani, and M. Kurt, "High Resolution MR Elastography Of The Human Brain: Technical Development And Applications In Aging And Alzheimer's Disease," in *Summer Biomechanics, Bioengineering and Biotransport Conference* 2023, Vail, CO, USA, Jun. 2023.
- [61] M. S. Hansen and T. S. Sørensen, "Gadgetron: An open source framework for medical image reconstruction," *Magn Reson Med*, vol. 69, no. 6, pp. 1768–1776, 2013, doi: 10.1002/mrm.24389.
- [62] B. Guérin *et al.*, "The Ultimate Signal-to-Noise Ratio in Realistic Body Models," *Magn. Reson. Med.*, vol. 5, no. 78, pp. 1969–1980, 2017, doi: 10.1002/mrm.26564.
- [63] P. Balchandani and T. P. Naidich, "Ultra-high-field MR neuroimaging," *American Journal of Neuroradiology*, vol. 36, no. 7, pp. 1204–1215, 2015, doi: 10.3174/ajnr.A4180.
- [64] K. Uğurbil *et al.*, "Ultrahigh field magnetic resonance imaging and spectroscopy," *Magn Reson Imaging*, vol. 21, no. 10, pp. 1263–1281, 2003, doi: 10.1016/j.mri.2003.08.027.
- [65] A. M. Peters *et al.*, "T2* measurements in human brain at 1.5, 3 and 7 T," *Magn Reson Imaging*, vol. 25, no. 6, pp. 748–753, 2007, doi: 10.1016/j.mri.2007.02.014.
- [66] S. Hirsch, J. Braun, and I. Sack, *Magnetic Resonance Elastography: Physical Background and Medical Applications*. 2017. doi: 10.1038/nm0596-601.
- [67] M. A. Griswold *et al.*, "Generalized Autocalibrating Partially Parallel Acquisitions (GRAPPA)," *Magn Reson Med*, vol. 47, no. 6, 2002, doi: 10.1002/mrm.10171.
- [68] S. J. Inati, M. S. Hansen, and P. Kellman, "A Fast Optimal Method for Coil Sensitivity Estimation and Adaptive Coil Combination for Complex Images," in *Proc. Intl. Soc. Meg. Reson. Med.*, 2014, p. 4407.

- [69] S. J. Inati, M. S. Hansen, and P. Kellman, "A Solution to the Phase Problem in Adaptive Coil Combination," in *Proc. Intl. Soc. Mag. Reson. Med.*, 2013, p. 2672.
- [70] A. Karsa and K. Shmueli, "SEGUE: A Speedy rEgion-Growing Algorithm for Unwrapping Estimated Phase," *IEEE Trans Med Imaging*, vol. 38, no. 6, pp. 1347–1357, 2019, doi: 10.1109/TMI.2018.2884093.
- [71] J. L. R. Andersson and S. N. Sotiropoulos, "An integrated approach to correction for off-resonance effects and subject movement in diffusion MR imaging," *Neuroimage*, vol. 125, pp. 1063–1078, Jan. 2016, doi: 10.1016/j.neuroimage.2015.10.019.
- [72] M. D. J. McGarry, E. E. W. Van Houten, P. R. Perriez, A. J. Pattison, J. B. Weaver, and K. D. Paulsen, "An octahedral shear strain-based measure of SNR for 3D MR elastography," *Phys Med Biol*, vol. 56, no. 13, 2011, doi: 10.1088/0031-9155/56/13/N02.
- [73] W. Penny, K. Friston, J. Ashburner, S. Kiebel, and T. Nichols, *Statistical Parametric Mapping: The Analysis of Functional Brain Images*, 1st Edition. 2006.
- [74] C. A. Chaze *et al.*, "Altered brain tissue viscoelasticity in pediatric cerebral palsy measured by magnetic resonance elastography," *Neuroimage Clin*, vol. 22, 2019, doi: 10.1016/j.nicl.2019.101750.
- [75] A. Manduca *et al.*, "MR elastography: Principles, guidelines, and terminology," May 01, 2021, *John Wiley and Sons Inc.* doi: 10.1002/mrm.28627.
- [76] E. R. Triolo *et al.*, "Design, Construction, and Implementation of a Magnetic Resonance Elastography Actuator for Research Purposes," *Curr Protoc*, vol. 2, no. 3, pp. 1–26, 2022, doi: 10.1002/cpz1.379.
- [77] S. Mohammed, P. Kozlowski, and S. Salcudean, "Phase-regularized and displacement-regularized compressed sensing for fast magnetic resonance elastography," *NMR Biomed*, vol. 36, no. 7, Jul. 2023, doi: 10.1002/nbm.4899.
- [78] X. Shan, J. Yang, P. Xu, L. Hu, and H. Ge, "Deep neural networks for magnetic resonance elastography acceleration in thermal-ablation monitoring," *Med Phys*, vol. 49, no. 3, pp. 1803–1813, Mar. 2022, doi: 10.1002/mp.15471.
- [79] H. Herthum *et al.*, "In vivo stiffness of multiple sclerosis lesions is similar to that of normal-appearing white matter," *Acta Biomater*, vol. 138, pp. 410–421, 2022, doi: 10.1016/j.actbio.2021.10.038.
- [80] S. Trattnig *et al.*, "Key clinical benefits of neuroimaging at 7 T," *Neuroimage*, vol. 168, pp. 477–489, Mar. 2018, doi: 10.1016/j.neuroimage.2016.11.031.
- [81] S. F. Svensson *et al.*, "Robustness of MR Elastography in the Healthy Brain: Repeatability, Reliability, and Effect of Different Reconstruction Methods," *Journal of Magnetic Resonance Imaging*, vol. 53, no. 5, pp. 1510–1521, 2021, doi: 10.1002/jmri.27475.
- [82] C. L. Johnson *et al.*, "Viscoelasticity of subcortical gray matter structures," *Hum Brain Mapp*, vol. 37, no. 12, pp. 4221–4233, 2016, doi: 10.1016/j.physbeh.2017.03.040.

- [83] G. McIlvain, A. M. Cerjanic, A. G. Christodoulou, M. D. J. McGarry, and C. L. Johnson, "OSCILLATE: A low-rank approach for accelerated magnetic resonance elastography," *Magn Reson Med*, vol. 88, no. 4, pp. 1659–1672, Oct. 2022, doi: 10.1002/mrm.29308.
- [84] D. R. Smith *et al.*, "Anisotropic mechanical properties in the healthy human brain estimated with multi-excitation transversely isotropic MR elastography," *Brain Multiphys*, vol. 3, 2022, doi: 10.1016/j.brain.2022.100051.
- [85] "QIBA Profile: Magnetic Resonance Elastography of the Liver 5 Stage 2: Consensus Profile," 2018.
- [86] S. K. Venkatesh, M. Yin, and R. L. Ehman, "Magnetic Resonance Elastography of Liver: Technique, Analysis and Clinical Applications," *J Magn Reson Imaging*, vol. 37, no. 3, pp. 544–555, 2013, doi: 10.1002/jmri.23731.Magnetic.
- [87] H. Morisaka *et al.*, "Magnetic resonance elastography is as accurate as liver biopsy for liver fibrosis staging," *Journal of Magnetic Resonance Imaging*, vol. 47, no. 5, pp. 1268–1275, 2018.
- [88] E. Ozkaya *et al.*, "Precision and Test-Retest Repeatability of Stiffness Measurement with MR Elastography: A Multicenter Phantom Study," *Radiology*, vol. 311, no. 2, May 2024, doi: 10.1148/radiol.233136.
- [89] A. Coelho and N. Sousa, "Magnetic resonance elastography of the ageing brain in normal and demented populations: A systematic review," Sep. 01, 2022, *John Wiley and Sons Inc.* doi: 10.1002/hbm.25891.
- [90] G. McIlvain, "The Role of the Viscous-to-Elastic Ratio in Brain Function & Samp; Health," Brain Commun, 2024.
- [91] D. A. Conroy, A. J. Spielman, and R. Q. Scott, "Daily rhythm of cerebral blood flow velocity," *J Circadian Rhythms*, vol. 3, Mar. 2005, doi: 10.1186/1740-3391-3-3.
- [92] S. Hetzer *et al.*, "Perfusion alters stiffness of deep gray matter," *Journal of Cerebral Blood Flow and Metabolism*, vol. 38, no. 1, pp. 116–125, Jan. 2018, doi: 10.1177/0271678X17691530.
- [93] B. M. Sandroff, C. L. Johnson, and R. W. Motl, "Exercise training effects on memory and hippocampal viscoelasticity in multiple sclerosis: a novel application of magnetic resonance elastography," *Neuroradiology*, vol. 59, no. 1, pp. 61–67, 2017, doi: 10.1007/s00234-016-1767-x.
- [94] B. Kreft *et al.*, "Cerebral Ultrasound Time-Harmonic Elastography Reveals Softening of the Human Brain Due to Dehydration," *Front Physiol*, vol. 11, Jan. 2021, doi: 10.3389/fphys.2020.616984.
- [95] S. Gholampour, "Feasibility of assessing non-invasive intracranial compliance using FSI simulation-based and MR elastography-based brain stiffness," *Sci Rep*, vol. 14, no. 1, Dec. 2024, doi: 10.1038/s41598-024-57250-4.
- [96] Z. Yin, A. J. Romano, A. Manduca, R. L. Ehman, and J. Huston, "Stiffness and beyond: What MR elastography can tell us about brain structure and function under physiologic and pathologic conditions," 2018, *Lippincott Williams and Wilkins*. doi: 10.1097/RMR.00000000000178.
- [97] F. V. Farahani *et al.*, "Effects of chronic sleep restriction on the brain functional network, as revealed by graph theory," *Front Neurosci*, vol. 13, no. OCT, 2019, doi: 10.3389/fnins.2019.01087.

- [98] M. L. Jackson *et al.*, "The effect of sleep deprivation on BOLD activity elicited by a divided attention task," *Brain Imaging Behav*, vol. 5, no. 2, pp. 97–108, Jun. 2011, doi: 10.1007/s11682-011-9115-6.
- [99] A. Arani *et al.*, "Acute pressure changes in the brain are correlated with MR elastography stiffness measurements: initial feasibility in an in vivo large animal model," *Magn Reson Med*, vol. 79, no. 2, pp. 1043–1051, Feb. 2018, doi: 10.1002/mrm.26738.
- [100] N. Zhang, J. Zhang, S. Du, and G. Ma, "Dehydration and rehydration affect brain regional density and homogeneity among young male adults, determined via magnetic resonance imaging: A pilot self-control trial," *Front Nutr*, vol. 9, Sep. 2022, doi: 10.3389/fnut.2022.906088.
- [101] P. Balchandani, M. M. Khalighi, G. Glover, J. Pauly, and D. Spielman, "Self-refocused adiabatic pulse for spin echo imaging at 7 T," *Magn Reson Med*, vol. 67, no. 4, pp. 1077–1085, 2012, doi: 10.1002/mrm.23089.
- [102] L. V. Hiscox *et al.*, "Hippocampal viscoelasticity and episodic memory performance in healthy older adults examined with magnetic resonance elastography," *Brain Imaging Behav*, vol. 14, no. 1, pp. 175–185, 2020, doi: 10.1007/s11682-018-9988-8.
- [103] P. L. Delgorio *et al.*, "Structure–Function Dissociations of Human Hippocampal Subfield Stiffness and Memory Performance," *Journal of Neuroscience*, vol. 42, no. 42, pp. 7957–7968, Oct. 2022, doi: 10.1523/JNEUROSCI.0592-22.2022.
- [104] S. A. Kruse *et al.*, "Magnetic resonance elastography of the brain," *Neuroimage*, vol. 39, no. 1, pp. 231–237, 2008, doi: 10.1016/j.neuroimage.2007.08.030.
- [105] G. Page *et al.*, "Multiresolution MR elastography reconstruction and comparison of different direct inversion algorithms in the liver," in *ISMRM & ISMRT Annual Meeting and Exhibition 2022*, 2022.
- [106] S. Papazoglou, U. Hamhaber, J. Braun, and I. Sack, "Algebraic Helmholtz inversion in planar magnetic resonance elastography," *Phys Med Biol*, vol. 53, no. 12, pp. 3147–3158, Jun. 2008, doi: 10.1088/0031-9155/53/12/005.
- [107] M. McGarry, E. Van Houten, L. Solamen, S. Gordon-Wylie, J. Weaver, and K. Paulsen, "Uniqueness of poroelastic and viscoelastic nonlinear inversion MR elastography at low frequencies," *Phys Med Biol*, vol. 64, no. 7, 2019, doi: 10.1088/1361-6560/ab0a7d.
- [108] W. Zeng et al., "Nonlinear Inversion MR Elastography with Low-Frequency Actuation," *IEEE Trans Med Imaging*, vol. 39, no. 5, pp. 1775–1784, 2020, doi: 10.1109/TMI.2019.2958212.
- [109] G. McIlvain, M. D. J. McGarry, and C. L. Johnson, "Quantitative effects of off-resonance related distortion on brain mechanical property estimation with magnetic resonance elastography," *NMR Biomed*, vol. 35, no. 1, Jan. 2022, doi: 10.1002/nbm.4616.
- [110] S. Ma *et al.*, "MR Elastography with Optimization-Based Phase Unwrapping and Traveling Wave Expansion-Based Neural Network (TWENN)," *IEEE Trans Med Imaging*, vol. 42, no. 9, pp. 2631–2642, 2023, doi: 10.1109/TMI.2023.3261346.

- [111] R. Wang *et al.*, "Fast magnetic resonance elastography with multiphase radial encoding and harmonic motion sparsity based reconstruction," *Phys Med Biol*, vol. 67, no. 2, 2022, doi: 10.1088/1361-6560/ac4a42.
- [112] S. Qiu *et al.*, "An electromagnetic actuator for brain magnetic resonance elastography with high frequency accuracy," *NMR Biomed*, vol. 34, no. 12, pp. 1–17, 2021, doi: 10.1002/nbm.4592.
- [113] K. J. Streitberger *et al.*, "How tissue fluidity influences brain tumor progression," *Proc Natl Acad Sci U S A*, vol. 117, no. 1, pp. 128–134, 2020, doi: 10.1073/pnas.1913511116.
- [114] M. McGarry *et al.*, "Mapping heterogenous anisotropic tissue mechanical properties with transverse isotropic nonlinear inversion MR elastography," *Med Image Anal*, vol. 78, May 2022, doi: 10.1016/j.media.2022.102432.
- [115] A. J. Hannum, G. McIlvain, D. Sowinski, M. D. J. McGarry, and C. L. Johnson, "Correlated noise in brain magnetic resonance elastography," *Magn Reson Med*, vol. 87, no. 3, pp. 1313–1328, Mar. 2022, doi: 10.1002/mrm.29050.
- [116] J. Veraart, E. Fieremans, and D. S. Novikov, "Diffusion MRI noise mapping using random matrix theory," *Magn Reson Med*, vol. 76, no. 5, pp. 1582–1593, Nov. 2016, doi: 10.1002/mrm.26059.